The non steady-state growth of divergent pearlite in Fe-C-Mn steels: A phase-field investigation

L.T. Mushongera[a,**], P. G. Kubendran Amos[b,**], E. Schoof[b], P. Kumar[a], B. Nestler[b,c]

[a]Department of Chemical & Materials Engineering,
University of Nevada Reno,USA
[b]Institute of Applied Materials (IAM-CMS), Karlsruhe Institute of Technology (KIT),
Strasse am Forum 7, 76131 Karlsruhe, Germany
[c]Institute of Digital Materials Science (IDM), Karlsruhe University of Applied Sciences,
Moltkestr. 30, 76133 Karlsruhe, Germany

Abstract

The eutectoid decomposition of austenite is generally analysed as a steady-state transformation. Although such a time-invariant framework is appropriate for binary systems, in ternary Fe-C-Mn alloys, particularly in the three-phase regime, a characteristic non-stationary equilibrium condition results in the formation of a unique microstructure, called 'divergent pearlite'. In the present work, the isothermal growth of the divergent pearlite, under different transformation temperatures; 605℃, 625℃ and 650℃, is investigated by adopting a phase-field approach which establishes local-equilibrium (LE) condition across the interface. Though most theoretical approaches intend to setup such condition, the current numerical technique elegantly recovers the non-stationary partitioning equilibrium (P-LE). The thermodynamical framework, which dictates this unique equilibrium condition, is introduced by incorporating the CALPHAD-based data. In addition to rendering the microstructure which is consistent with the observed divergent-pearlite, the factors governing the characteristic kinetics and phase distributions are analysed. In complete agreement with the existing studies, it is recognised that the non steady-state growth is induced by a proportional decrease in the matrix carbon-content, which reduces the transformation kinetics, by influencing the Mn partitioning driving-force. The characteristic proportionality which exists between these governing factors is unraveled in the current investigation. Moreover, it is also identified that the transition from the non steady-state evolution in three-phase regime to predominantly steady state in two-phase regime, is continuous. In other words, at

higher undercooling, a resolvable segment of time-invariant growth is observed in the initial stages, which is subsequently followed by the divergent evolution.

1. Introduction

Eutectoid transformation primarily involves decomposition of a solid phase into two different solid phases. The resulting phases often grow cooperatively, thereby yielding a lamellar microstructure. In steels, the eutectoid decomposition of austenite yields an inter-twinned bicrystal of ferrite and cementite, which is referred to as pearlite [1]. Owing to the extensive applicability of pearlite [2], the responsible phase transformation has extensively been analysed for decades. In addition to the experimental investigations, the eutectoid decomposition in steels have also been theoretically studied [3, 4]. One fundamental requirement for analysing any phase transformation is the realisation of the equilibrium composition of the phases, as it defines the driving force and position of the interface. For instance, assuming the local equilibrium condition [5], the position of the interface during the growth of ferrite in a binary system can be expressed as

$$(c_{C:eq}^{\gamma} - c_{C:eq}^{\alpha})\frac{\mathrm{d}s}{\mathrm{d}t} = -J_{C}, \tag{1}$$

where the equilibrium composition of ferrite and austenite are correspondingly represented by $c_{C:eq}^{\alpha}$ and $c_{C:eq}^{\gamma}$. In Eqn. 1, the velocity of the interface is written as $\mathrm{d}s/\mathrm{d}t$, while J_{C} denotes the flux of the carbon. With one independent concentration, the equilibrium composition of the phases in a binary system can directly be determined by considering a tie-line which passes through the initial matrix composition. Therefore, by substituting this characteristic concentration, the kinetics of the transformation can be ascertained through Eqn. 1. However, the theoretical treatment gets convoluted when additional alloying elements are introduced.

*L.T. Mushongera

**P G Kubendran Amos

Email addresses: `lmushongera@unr.edu` (L.T. Mushongera), `prince.amos@kit.edu` (P. G. Kubendran Amos)

From Eqn. 1, it can be deduced that the interface velocity in a ternary system depends on the flux of the two independent components. In Fe-C-Mn steel, the flux of the alloying elements [6], carbon and manganese, is respectively written as

$$- J_{\mathrm{C}} = \sum_{\alpha} D_{\mathrm{C}}^{\alpha} \boldsymbol{\nabla} c_{\mathrm{C}} + D_{\mathrm{C:Mn}}^{\alpha} \boldsymbol{\nabla} c_{\mathrm{Mn}} \tag{2}$$

$$- J_{\mathrm{Mn}} = \sum_{\alpha} D_{\mathrm{Mn}}^{\alpha} \boldsymbol{\nabla} c_{\mathrm{Mn}} + D_{\mathrm{Mn:C}}^{\alpha} \boldsymbol{\nabla} c_{\mathrm{C}}. \tag{3}$$

It is evident from the above expression that, in addition to the gradient in the concentrations, $\boldsymbol{\nabla} c_{\mathrm{C}}$ and $\boldsymbol{\nabla} c_{\mathrm{Mn}}$, the flux is governed by the diffusivities of the components which include the ternary interactions, $D_{\mathrm{C:Mn}}^{\alpha}$ and $D_{\mathrm{Mn:C}}^{\alpha}$. Since carbon occupies the interstitial sites and the manganese atoms replaces iron in the regular lattice, the diffusivities of these components are noticeably different, $D_{\mathrm{C}}^{\alpha} \boldsymbol{\nabla} c_{\mathrm{C}} >> D_{\mathrm{Mn}}^{\alpha} \boldsymbol{\nabla} c_{\mathrm{Mn}}$. The significant disparity in the diffusion coefficients introduces a complexity in analysing the transformation rate. Therefore, a thermodynamic framework which includes two definite local equilibrium conditions, referred to as partitioning- (P-LE) and negligible partitioning-local equilibrium (NP-LE), is considered to investigate the transformation kinetics in Fe-C-Mn system [7, 8, 9, 10]. Moreover, this framework has been extended to elucidate the formation of non-equilibrium phases and discontinuous porous-cementite [11, 12, 13].

The transformation under the partitioning-local equilibrium (P-LE) is governed by the partitioning of the slower diffusing species, manganese [14]. This is achieved by decreasing the driving force of the carbon migration substantially. In other words, the relative supersaturation of carbon under P-LE condition reads

$$\Gamma_{\mathrm{C}} = \frac{c_{\mathrm{C:eq}}^{\gamma} - c_{\mathrm{C}}^{\infty}}{c_{\mathrm{C:eq}}^{\gamma} - c_{\mathrm{C:eq}}^{\alpha}} \approx 0, \tag{4}$$

where c_{C}^{∞} is the matrix composition. On the other hand, under negligible partitioning-local equilibrium (NP-LE), the local driving force of the manganese is considerably increased to keep-in pace with the faster diffusing carbon. Correspondingly, the supersaturation of manganese under NP-LE pertains to

$$\Gamma_{\mathrm{Mn}} = \frac{c_{\mathrm{Mn:eq}}^{\gamma} - c_{\mathrm{Mn}}^{\infty}}{c_{\mathrm{Mn:eq}}^{\gamma} - c_{\mathrm{Mn:eq}}^{\alpha}} \approx 1. \tag{5}$$

The range of concentrations which satisfy Eqn. 4, with respect to the tie-line(s), in a two-phase ternary isotherm are treated as the partition region, while concentrations which fulfill Eqn. 5 pertain to the negligible-partition regime. In transformations involving three phases, like eutectoid decomposition, the P- and NP-LE conditions are distinguished by considering the overlap in the appropriate regions which are determined from the two phase setup [14]. In the present work, the microstructural evolution accompanying the growth 'partitioned' pearlite is studied by employing multicomponent multiphase-field approach.

In a conventional isothermal eutectoid transformation, the supersaturation primarily affects the kinetics of the evolution, while largely rendering regular lamellar microstructure. However, in the Fe-C-Mn system, owing to the unique thermodynamic framework, both the kinetics and microstructural evolution are significantly influenced by the composition. For instance, in two-phase P-LE regime, wherein the austenite completely transforms, the introduction of manganese noticeably reduces the evolution rate, for a given carbon concentration [15, 16, 17]. Additionally, it has been observed that, the interlamellar spacing of pearlite changes before the impingement of the nodules, thereby revealing a 'soft-impingement' in the carbon concentration, particularly, the C-depleted zone [18]. Relatively more interesting outcomes are reported to accompany the transformations in the three-phase P-LE regime, wherein the austenite is not entirely consumed.

The cooperative growth of the pearlite is generally treated as a steady-state transformation which is characterised by the constant growth-rate and time-invariant interlamellar spacing. However, the austenite decomposition in the three-phase P-LE regime deviates significantly form these characterising factors and therefore, exhibits a non steady-state evolution [18]. In other words, the distance between the cementite structure progressively increases with the transformation, while the growth rate decreases. The resulting microstructure is referred to as the 'divergent pearlite' [19]. In view of the thermodynamic framework elucidated above, and assuming the absence of long-range manganese diffusion, the formation of the divergent pearlite is attributed to the gradual change in the average carbon-content in the parent phase, austenite [14, 9, 10]. The reduction in the average carbon-concentration minimises the driving force for the partitioning of manganese and thus, decreases the transformation rate. Furthermore, the decrease in the carbon composition concomitantly leads to an increase in the interlamellar spacing.

4

Experimentally investigating the argument which undergirds the formation of the divergent pearlite is an arduous task, as it involves tracking the average composition of austenite during the transformation. However, the concentration across the interface has been monitored to describe the governing factor [18, 20, 21]. Consistent with the thermodynamic framework, it has been identified that the supersaturation of manganese at the growth front decreases with the time and the slow diffusing species exhibit no long-range diffusion. Despite these observations, a comprehensive understanding of the temporal evolution of the individual components, and their influence on the growth of the divergent pearlite, has not been achieved yet. Therefore, in the present work, a phase-field approach which facilitates the incorporation of CALPHAD data and more importantly, establishes non-stationary local-equilibrium condition is adopted to extensively analyse the changes in the composition accompanying the non steady-state eutectoid transformation [22].

In a conventional numerical treatment, referred to as the sharp-interface approach, the task of tracking the interface gets increasingly complicated with the shape and number of components [4, 23]. The phase-field technique circumvents this complexity by introducing an additional scalar variable, called phase field, which assumes a constant value in the bulk phase, while exhibiting the smooth transition across the interface. Although the transition of the phase field replaces the sharp interface with a diffuse one, the need for tracking the interface is averted, as the microstructural changes is now reflect by the spatio-temporal changes in the scalar variable. Moreover, it has been shown through asymptotic analysis that the phase-field model recovers sharp-interface solutions, despite the diffuse interface [24, 25]. The phase-field technique has been adopted to numerically investigate both solidification and solid-state transformations [26, 27], including eutectoid decomposition [28, 29], and curvature-driven evolutions [30, 31, 32, 33, 34]. However, except for the previous work of the present authors, not much has been reported on the non steady-state transformation using this technique. Therefore, the initial studies in Ref. [22] are extended to unravel the underpinning changes in the concentrations which yield divergent pearlite.

2. Simulation setup

The quantitative nature of any phase-field model relies on its ability to efficiently decouple the contributions of the interface and the bulk phases. In a multicomponent system, this is achieved by considering the chemical potential as the continuous variable [35, 24]. Despite being treated as the continuous variable, the chemical potential is rarely used as a constitutive-dynamic parameter. In this study, a model which employs the chemical potential as a dynamic variable is adopted for computational efficiency, since more than one independent concentration-variable is involved. Although a descriptive elucidation of the model is rendered elsewhere [22], a contextual delineation is presented in this section.

2.1. Multicomponent phase-field model

In the present model, the overall energy density of a system, which includes multiple bulk phases and corresponding diffuse interfaces, is written in the form of the Ginzburg-Landau functional as

$$\Omega(T, \boldsymbol{\mu}, \boldsymbol{\phi}) = \int_V \left[\left(\epsilon \tilde{a}(\boldsymbol{\phi}, \nabla \boldsymbol{\phi}) + \frac{1}{\epsilon} \tilde{w}(\boldsymbol{\phi}) + \Psi(T, \boldsymbol{\mu}, \boldsymbol{\phi}) \right) \right] \mathrm{d}V, \tag{6}$$

where the first two terms on the right hand side of the functional represent the contribution of the interface while the remaining term introduces the bulk contribution. Particularly, $\tilde{a}(\boldsymbol{\phi}, \nabla \boldsymbol{\phi})$ is the gradient energy term while $\tilde{w}(\boldsymbol{\phi})$ is the obstacle-type potential. In order enhance the numerical efficiency of the approach, the grand potential density, $\Psi(T, \boldsymbol{\mu}, \boldsymbol{\phi})$, which considers chemical potential as the dynamic variable, is adopted to introduce the chemical contribution of the bulk phases. Owing to the multicomponent and multiphase considerations, both the phase field and chemical potential are correspondingly represented by N- and K-tuple vector variable $\boldsymbol{\phi}$ and $\boldsymbol{\mu}$, where N and K are number of phases and components, respectively. Moreover, the contribution of the multiple phases to the overall grand-potential density of the system is expressed as

$$\Psi(T, \boldsymbol{\mu}, \boldsymbol{\phi}) = \sum_{\alpha=1}^{N} \Psi_\alpha(T, \boldsymbol{\mu}) h_\alpha(\boldsymbol{\phi}), \tag{7}$$

where h_α is the interpolation function of the form $h_\alpha(\phi) = \phi_\alpha^2(3 - 2\phi_\alpha)$. The individual grand-potential density is the Legendre transform of its corresponding free-energy density [36], which

reads

$$\Psi^\alpha(T, \boldsymbol{\mu}) = f^\alpha(\boldsymbol{c}^\alpha(T, \boldsymbol{\mu})) - \sum_{i=1}^{K-1} \mu_i c_i^\alpha(T, \boldsymbol{\mu}), \tag{8}$$

where $\boldsymbol{c}^\alpha$ is the discontinuous K-tuple vector representing the phase-dependent concentration in mole fraction.

The temporal evolution of the phase field is governed by the phenomenological change in the functional expressed in Eqn. 6. Correspondingly, the evolution of the phase field is written as

$$\tau\epsilon\frac{\partial\phi_\alpha}{\partial t} = \epsilon\left(\nabla\cdot\frac{\partial\tilde{a}(\boldsymbol{\phi}, \nabla\boldsymbol{\phi})}{\partial\nabla\phi_\alpha} - \frac{\partial\tilde{a}(\boldsymbol{\phi}, \nabla\boldsymbol{\phi})}{\partial\phi_\alpha}\right) - \frac{1}{\epsilon}\frac{\partial\tilde{w}(\boldsymbol{\phi})}{\partial\phi_\alpha}$$
$$- \frac{\partial\Psi(T, \boldsymbol{\mu}, \boldsymbol{\phi})}{\partial\phi_\alpha} - \Lambda, \tag{9}$$

where Λ is Lagrange multiplier which imposes the multiphase-field constraint, $\sum_{\alpha=1}^{N}\phi_\alpha = 1$, and τ is the relaxation constant. As indicated in Eqn. 9, the temporal changes in the phase field is governed by the chemical potential. By considering the conservative evolution of the concentration of species i, the temporal change in the chemical potential is expressed as

$$\frac{\partial\mu_i}{\partial t} = \left[\underbrace{\nabla\cdot\sum_{j=1}^{k-1}\boldsymbol{M}_{ij}(\boldsymbol{\phi})\nabla\mu_j}_{\frac{\partial c_i}{\partial t}} - \sum_\alpha^N c_i^\alpha(\boldsymbol{\mu}, t)\frac{\partial h_\alpha(\boldsymbol{\phi})}{\partial t}\right]\left[\sum_\alpha^N \mathcal{X}_{ij}(\boldsymbol{\phi})\right]^{-1}, \tag{10}$$

where, owing to the multicomponent nature of the system, the mobility is represented by the $\boldsymbol{M}_{ij}(\boldsymbol{\phi})$ matrix which appends the CALPHAD-based diffusivity matrix. And $\mathcal{X}_{ij}(\boldsymbol{\phi})$ is the susceptibility matrix, darken factor, which ensures that the diffusivity is constant within a phase.

In the present multicomponent numerical approach, the chemical potentials which are interpolated across the diffuse interface are equilibrated consistently with its thermodynamic conditions [24, 37]. In a conventional sense, although this interpolation averts the influence of the bulk phases on the interface and recovers the sharp interface kinetics, it establishes local equilibrium across the interface during the phase transformation. Therefore, when the CALPHAD parameter associated with the P-LE regime are introduced, the model inherently establishes the corresponding equilibrium condition. In other words, upon incorporating appropriate parameters, the evolution of the phase field and the governing variables adhere to the P-LE condition.

Table 1: CALPHAD-retrieved diffusivity matrix incorporated in the model

	605°C		625°C		650°C	
D_{ij}^{γ}	C	Mn	C	Mn	C	Mn
C	1.31×10^{-13}	-1.47×10^{-14}	1.32×10^{-13}	1.52×10^{-14}	3.13×10^{-11}	-5.74×10^{-14}
Mn	1.56×10^{-21}	7.71×10^{-21}	-1.63×10^{-21}	6.23×10^{-21}	-9.05×10^{-19}	1.34×10^{-18}
D_{ij}^{α,M_3C}	C	Mn	C	Mn	C	Mn
C	2.56×10^{-11}	-4.63×10^{-12}	3.13×10^{-11}	-5.74×10^{-14}	4.81×10^{-11}	-1.04×10^{-16}
Mn	-4.34×10^{-19}	1.17×10^{-18}	-9.05×10^{-19}	1.34×10^{-18}	-1.71×10^{-18}	1.54×10^{-17}

Table 2: Phase-dependent susceptibility-matrix

	605°C			625°C			650°C		
	α	γ	M_3C	α	γ	M_3C	α	γ	M_3C
$\mathcal{X}_C^{\Theta}$	93365100	486303	120690800	60345400	441955	120690800	36283800	397984	120690800
$\mathcal{X}_{Mn}^{\Theta}$	251175	68306.4	587652	293826	80654.5	322200	380567	104843	587652

Since recent experimental investigations have shown that local equilibrium is established across the interface during the pearlite transformation, in both two- and three-region, the introduction of the P-LE condition enhances the physicality of this treatment [18, 20, 21].

2.2. Domain configuration

For the current analysis, eutectoid transformations in Fe-$2.51at.\%$C-$5.40at.\%$Mn steel is considered at three different temperatures; 605°C, 625°C and 650°C. As shown in the Fig. 1, this con-
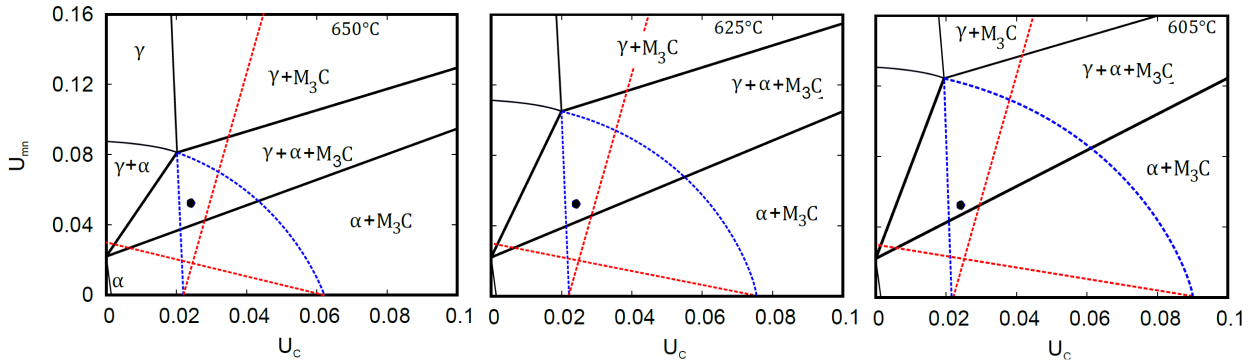

Figure 1: Isothermal sections of the Fe-C-Mn phase diagram at 650°C, 625°C and 605°C. The solid circles show the alloy composition which lies in the three phase region.

Table 3: List of simulation parameters and material constant.

Parameter	Value	Unit
Relaxation parameter ($\tau_{\alpha\gamma}$)	1.72×10^9	Jsm^{-4}
Relaxation parameter ($\tau_{M_3C\gamma}$)	7.1×10^9	Jsm^{-4}
Grid size ($\Delta X = \Delta Y$)	0.42	μm
Length-scale parameter (ε)	$3 \times \Delta X$	μm
Domain size	450×450	μm $\times$ μm
Molar volume ($\tilde{\Omega}$)	7.16482×10^{-6}	m^3/mole
Interfacial Energy ($\sigma_{\alpha\gamma} = \sigma_{\alpha M_3C} = \sigma_{\gamma M_3C}$)	0.49	Jm^{-2}

centration denoted by the solid circles pertains to the three-phase regime above the P- and NP-LE transition line, at the temperatures considered. Moreover, it is evident that the concentration is close to two-phase regime at 605℃. It is important to realise that, for this illustration alone, the concentrations are expressed in U-fraction, which is $U_i = c_i/(1 - c_C)$.

The appropriate free energies of the phases and the chemical potentials of the components are introduced based on data from the TCFE8-database, via Thermocalc, through the polynomial approximation technique. Since the approach adopted for this incorporation has already been discussed in the previous work of the authors, the readers are directed to ref. [22, 38] for a comprehensive understanding. Moreover, the factors which govern the distribution of the components, like diffusivity and susceptibility matrix, are obtained from the kinetics database-MOBFE3 via Dictra. These kinetic parameters along with the other thermodynamic quantities associated with the transformation are tabulated in Tables. 1 and 2.

The simulation domain, which is confined to two-dimension, is discretised into uniform grids of dimension $\Delta X = \Delta Y = 0.42 \mu$m through the finite-difference scheme. Identical domains of size $450 \times 450 \mu$m are adopted for simulating the transformations at different temperatures. The width of the diffuse interface is fixed by assigning a constant value to the length parameter, ε. An interface with approximately six grid-points is devised by considering $\varepsilon = 3.0 \Delta X$. The factors associated with the simulation domain and the interface are presented in Table. 3. Using finite-difference approach, the equations which govern the evolution of the fundamental variables are
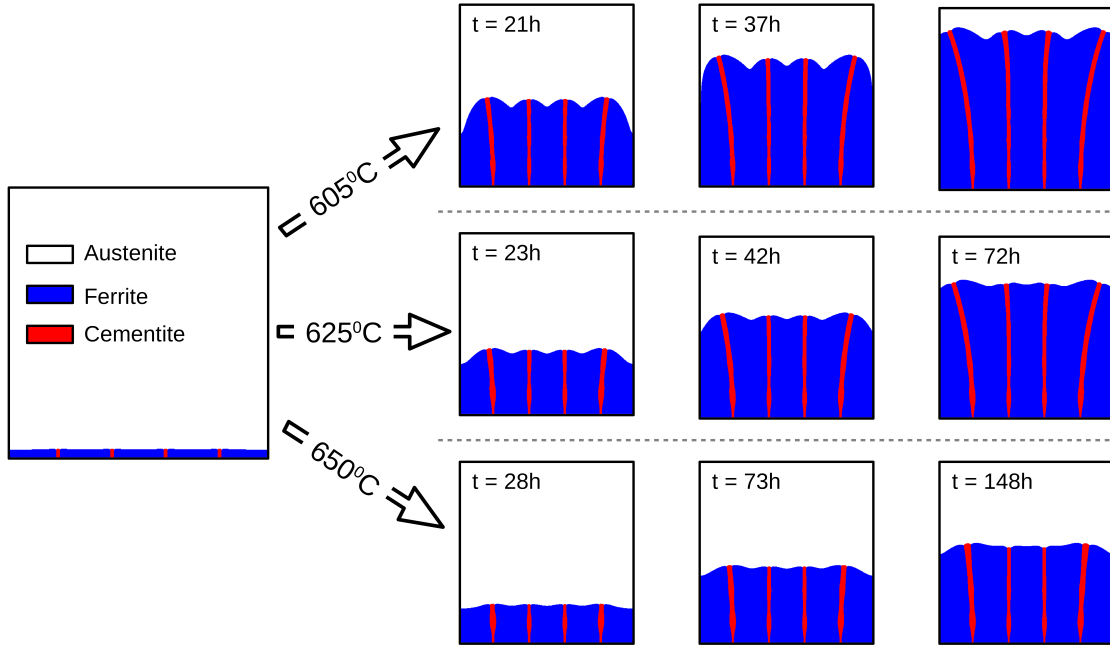
9

Figure 2: Three-phase simulation domain which predominantly comprises of austenite-matrix with ferrite and cementite bulk-phases arranged alternatively. The phase transformation resulting in the cooperative growth of the pearlite at three different temperatures (605°C, 625°C and 650°C) is included.

solved explicitly by the forward marching Euler scheme. While the no-flux Neumann boundary condition is imposed in the growing direction, periodic boundary conditions are assumed for the remaining sides. Moreover, the computational efficiency of the present technique is enhanced by employing the domain decomposition though the Message Passing Interface (MPI).

3. Results and discussion

The domain configuration considered for all the simulations in the present analysis is shown in Fig. 2. In order to render a comparative investigation, the systems are invariably initialised with an average composition of $c_C = 0.0250478$ and $c_{Mn} = 0.0539651$. Moreover, as shown in Fig. 2, the distribution of the phases in the early stage, particularly the interlamellar spacing, is fixed. Since the chemical composition of the system at all three temperatures is identical, and the isothermal transformation is exclusively studied, this setup is deemed reasonable.

Owing to the CALPHAD-based description of the free-energy density of the system, the alloy composition innately establishes the driving force for the 'partitioned' phase transformation,

governed by the appropriate equilibrium condition [22]. However, despite the similar concentration, significant disparity is anticipated in the microstructural evolution at different conditions, since the equilibrium condition, and consequently, the driving force, are dictated by the temperature.

3.1. Microstructural evolution

The microstructures resulting from the eutectoid transformation at temperatures 605°C, 625°C and 650°C, for similar domain setup, are illustrated in Fig. 2. Consistent with the position of the average concentration in the ternary isotherm, the phase-change ultimately yields a microstructure with a combination of the three phases; ferrite (α), cementite (M_3C) and austenite (γ). Furthermore, it is evident that the rate of transformation is visibly different for different temperatures. Specifically, the rate of austenite decomposition decreases with an increase in temperature. Despite the dissimilarity in the transformation rate, the pearlite in all the three conditions deviates from the conventional microstructure. In other words, as opposed to the lamellar arrangement of ferrite and cementite with a constant spacing, at the temperatures considered, the eutectoid transformations yield divergent pearlite, which is characterised by increasing distance between the cementite structures. Additionally, Fig. 2 unravels that the interlamellar spacing progressively increases till a chemical equilibrium is established between the phases. This microstructural evolution is qualitatively consistent with the experimental observations associated with the eutectoid transformation under similar thermodynamic conditions [19, 18, 21].

While all the transformations illustrated in Fig. 2 yield microstructures with the pearlite and austenite, the volume fractions of the constituent phases are noticeably different. Although the preliminary investigations explicating the thermodynamic consistency of the present numerical approach has been elucidated elsewhere [22], in order to quantitatively examine the incorporated thermodynamic quantities, the temporal change in the volume fraction of the phases are monitored during the austenite decomposition.

The CALPHAD-predicted influence of temperature on the volume fraction of the eutectoid-phases, in Fe-C-Mn system, is shown in Fig. 3a. The increase in the volume fraction of austenite with raise in temperature seemingly agrees with the microstructural changes illustrated in Fig. 2.
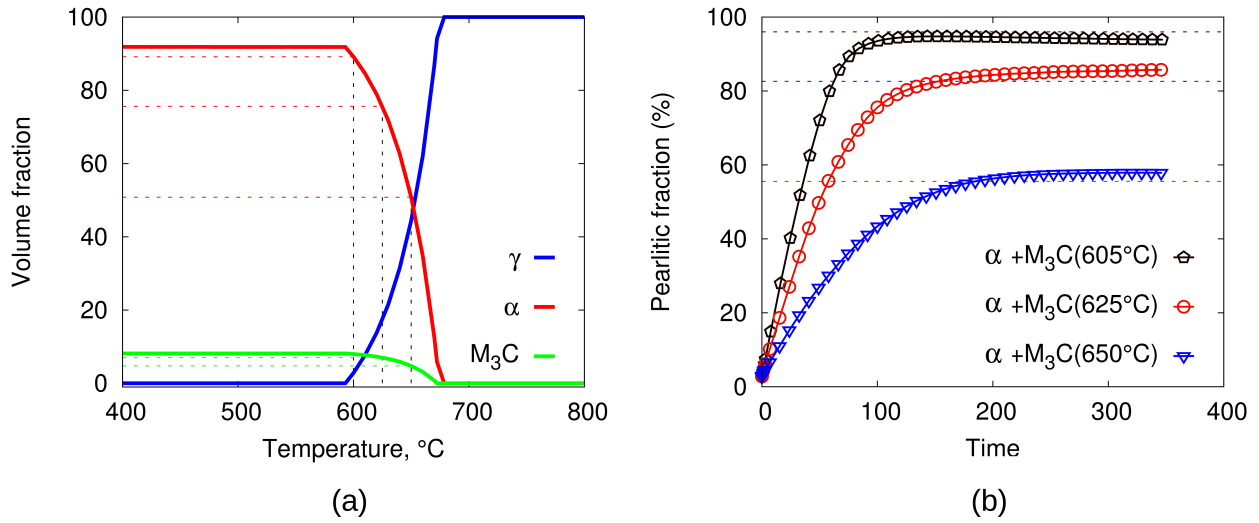
11

Figure 3: a) Influence of temperature on the equilibrium phase-fraction for a given concentration, in accordance with the CALPHAD database. b) Temporal change in the pearlite volume-fraction accompanying the growth of divergent pearlite at 605°C, 625°C and 650°C. The volume fraction predicted by the CALPHAD database is superimposed in the illustration.

However, to comprehensively compare the observed evolution with the CALPHAD predictions, the temporal change in the volume of pearlite is plotted in Fig. 3b, wherein the thermodynamically-anticipated quantities are overlayed. This illustration shows that the eutectoid transformations, which are characterised by a progressive increase in ferrite and cementite volume, eventually attain equilibrium with constant phase fractions. In all the three conditions studied, the phase fractions predicted by the current approach are in complete agreement with the CALPHAD data, as shown in Fig. 3b. Since this consistency in the volume fraction of the phases cannot be achieved without the incorporation appropriate driving-force, and the corresponding thermodynamic conditions at the interface, the illustration in Fig. 3b substantiates the quantitative nature of the current technique, albeit to a certain extent.

3.2. Growth kinetics

In addition to its unique microstructure, the divergent pearlite exhibits a non-conventional transformation kinetics. Based on the thermodynamical delineations alone, it has theoretically been claimed that growth of divergent pearlite is accompanied by a gradual decrease in the transformation rate [14, 9, 10]. Moreover, recent experimental investigations have definitively unrav-
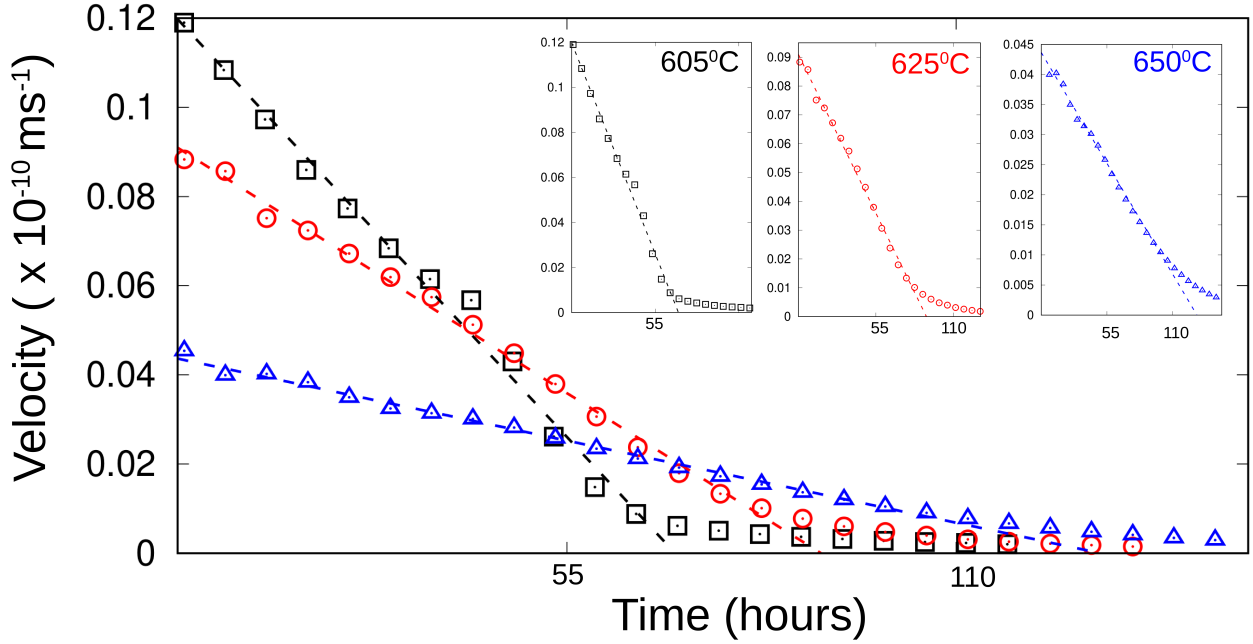
12

Figure 4: The temporal change in the averaged growth-rate accompanying the evolution of the divergent pearlite at different undercooling. The decrease in averaged growth-rate at temperatures 605℃, 625℃ and 650℃ are separately included as subplots.

eled a decelerating kinetics [18, 21]. To analyse the kinetics of the evolutions illustrated in Fig. 2, in view of these observations, the interface migration which establishes the phase-change is quantified.

The rate of any transformation can be ascertained by considering the temporal change in the volume of the emerging phase or by tracking the position of the corresponding interface. Often experimentally adopted techniques assume an ideal morphology for pearlite colonies to calculate the growth rate [39]. Since the shape of the nodule are noticeably different from the ideal structures, particularly in divergent pearlite, Cahn and Hagel (CH) developed an alternate approach which obviates any morphological consideration [19]. This technique has since been extensively employed to determine the kinetics of phase transformation [12, 40] and recrystallization [41, 42] Therefore, the growth rate of divergent pearlite is determined using the CH-technique in this study. The averaged growth-rate, according to CH-technique, is estimated by

$$\bar{v}_{\text{div}} = \frac{1}{S_{\text{p}}} \frac{\partial V_{\text{p}}}{\partial t} \tag{11}$$

13

where S_p is the interface area of the pearlite, which includes the interfaces separating ferrite and cementite from austenite. Moreover, in Eqn. 11, V_p represents the volume of the pearlite, its temporal change is denoted by $\frac{\partial V_\text{p}}{\partial t}$. In a multiphase-field model, owing to the constraint $\sum_{\alpha=1}^{N} \phi_\alpha = 1$, the phase field of an individual phase can be treated as its volume fraction in the system. Accordingly, the volume of the pearlite is calculated by

$$V_\text{p} = \int_V \left(\phi_\alpha + \phi_{M_3C} \right) \mathrm{d}V, \tag{12}$$

where ϕ_α and ϕ_{M_3C} are the scalar phase-field associated with ferrite and cementite, respectively. Furthermore, since a phase field assumes a definite value only within the corresponding bulk phase, the product of two different phase fields are non-zero in the interface alone. This characteristic feature of the phase-field technique is adopted to determine the interfacial area, which is written as

$$S_\text{p} = \frac{1}{\delta} \int_V \left(\phi_\alpha \phi_\gamma + \phi_{M_3C} \phi_\gamma \right) \mathrm{d}V, \tag{13}$$

where ϕ_γ is the scalar austenite phase-field. Owing to the diffuse nature of the interface, in Eqn 13, the interface width (ε) is introduced.

The temporal change in the transformation kinetics, calculated through the CH-technique, accompanying the austenite decomposition at different temperatures 605℃, 625℃ and 650℃ is plotted in Fig. 4. Moreover, in Fig. 4, the evolution of the averaged growth-rate at each temperature are separately included as subsets. The initial transformation rate are predominantly governed by the undercooling. Correspondingly, at the beginning of the evolution, the growth kinetics are visibly greater in transformation pertaining to 605℃, which is followed by the 625℃. The dependence of kinetic parameters on the temperature, in addition to the supersaturation, is responsible for the disparity in the initial stages of the austenite decomposition.

Consistent with the experimental observations [18], albeit qualitatively, the temporal change in the kinetics is predominantly linear irrespective of the undercooling. In other words, as shown in Fig. 4, the growth of the divergent pearlite is largely accompanied by a proportional (linear) decrease in the averaged interface-velocity, before gradually reaching the equilibrium phase-fractions. Although this characteristic decrease in kinetics is exhibited at all temperatures, the
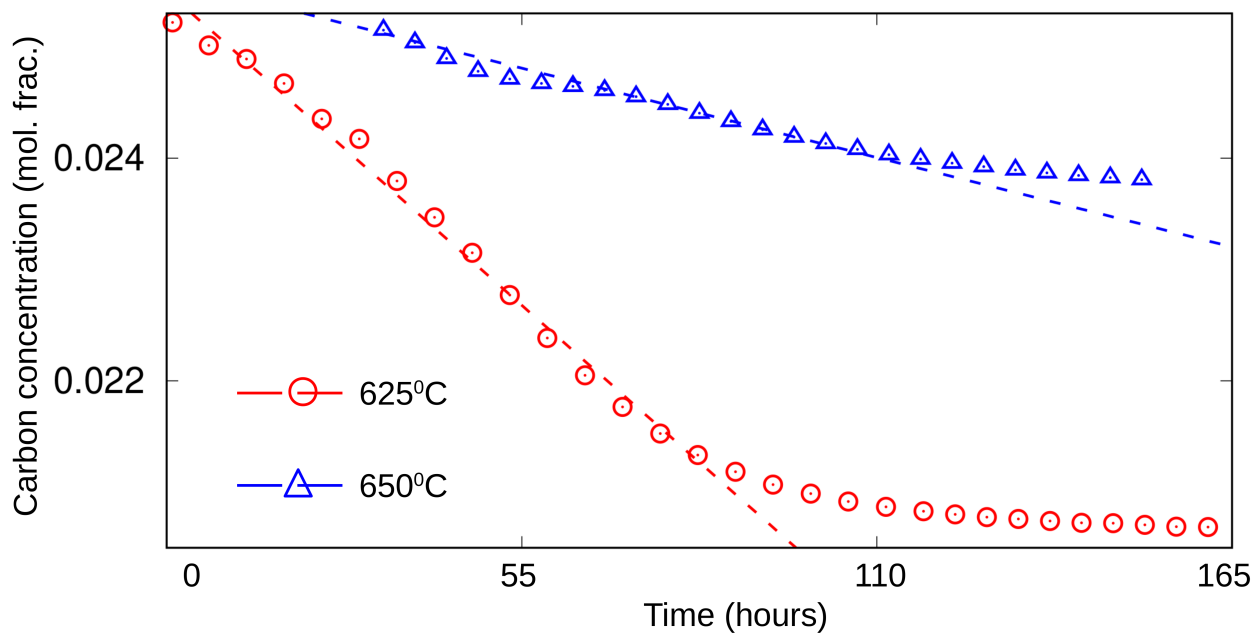
14

Figure 5: The progressive decrease in the austentite carbon-content during its decomposition at 625℃ and 650℃.

reduction rate is more pronounced at higher undercooling. For instance, the change in the aver-
aged growth-rate at 650℃, though primarily linear, is not significantly different from the gradual
transition to the equilibrium, which is observed at the final stages of the transformation. There-
fore, besides the initial kinetics, the rate of change in the growth velocity during the pearlite
growth is substantially influenced by the transformation temperature.

3.3. Evolution of carbon concentration

The progressive change in the matrix carbon-concentration underpins the non steady-state
kinetics and the characteristic microstructure associated with the divergent pearlite [14, 9, 10].
Owing to the complexities involved in monitoring this decrease in the austenite composition, the
consequent change in the equilibrium condition across the interface has been analysed experi-
mentally [18, 21]. Based on the non-stationary equilibrium conditions, the change in the matrix
carbon-concentration is explicated in these investigations. As opposed to the latent approach
in experiments for understanding the evolution of the austenite composition, the influence of
a temporal change in the corresponding carbon-content on kinetics and phase distribution is
directly investigated in this analysis.

15

As elucidated in Sec. 2.1, a unique feature of the present numerical technique is that the chemical potential of the components are treated as the dynamic variable. This consideration obviates the need for ascertaining the phase concentrations at every time-step, thereby enhancing the efficiency of the technique [36]. However, since the evolution of the austenite-concentration is pivotal for the present study, the corresponding concentrations are derived from the free-energy formulation.

As delineated in Ref. [22], the free-energy density of the phase-γ is expressed in the form of second-degree polynomial as

$$f^{\gamma}(c_{\mathrm{C}}, c_{\mathrm{Mn}}, T) = A^{\gamma}(T)c_{\mathrm{C}}^2 + B^{\gamma}(T)c_{\mathrm{Mn}}^2 + D^{\gamma}(T)(1 - c_{\mathrm{C}} - c_{\mathrm{Mn}})^2 \tag{14}$$
$$+ E^{\gamma}(T)c_{\mathrm{C}} + H^{\gamma}(T)c_{\mathrm{Mn}} + I^{\gamma}(T)(1 - c_{\mathrm{C}} - c_{\mathrm{Mn}}) + J^{\gamma}(T).$$

Since c_{C} and c_{Mn} respectively denote mole fraction of carbon and manganese, the remnant composition is represented by $c_{\mathrm{Fe}} = 1 - c_{\mathrm{C}} - c_{\mathrm{Mn}}$. The temperature-dependent coefficients, $A^{\gamma}(T)$, $B^{\gamma}(T)$, $D^{\gamma}(T)$, $E^{\gamma}(T)$, $H^{\gamma}(T)$, $I^{\gamma}(T)$ and $J^{\gamma}(T)$, are ascertained from CALPHAD database. According to this free-energy formulation, one of the continuous variable, the chemical potential of carbon (μ_{C}) is written as

$$\mu_{\mathrm{C}} = \frac{\partial f^{\gamma}(c_{\mathrm{C}}, c_{\mathrm{Mn}}, T)}{\partial c_{\mathrm{C}}} \tag{15}$$
$$= 2A^{\gamma}(T)c_{\mathrm{C}} + 2D^{\gamma}(T)(c_{\mathrm{C}} + c_{\mathrm{Mn}}) + \underbrace{E^{\gamma}(T) - 2D^{\gamma}(T) - I^{\gamma}(T)}_{:= \mathcal{T}_{\mathrm{C}}^{\gamma}}$$

From the above Eqn. 15, the phase-dependent carbon concentration governing the isothermal transformation can be estimated

$$c_{\mathrm{C}}^{\gamma} = \frac{1}{2}\left(\frac{\mu_{\mathrm{C}} - 2D^{\gamma}c_{\mathrm{Mn}}^{\gamma} - \mathcal{T}_{\mathrm{C}}^{\gamma}}{A^{\gamma} + D^{\gamma}}\right) \tag{16}$$

However, since the above relation involves unknown austenite manganese-composition (c_{Mn}), the other continuous variable associated with the phase-field formulation is determined from the austenite free-energy density described in Eqn.14. Correspondingly, the manganese chemical-

16

potential reads

$$\mu_{\mathrm{Mn}} = \frac{\partial f^{\gamma}(c_{\mathrm{C}}, c_{\mathrm{Mn}}, T)}{\partial c_{\mathrm{Mn}}} \tag{17}$$

$$= 2B^{\gamma}(T)c_{\mathrm{Mn}} + 2D^{\gamma}(T)(c_{\mathrm{C}} + c_{\mathrm{Mn}}) + \underbrace{H^{\gamma}(T) - 2D^{\gamma}(T) - J^{\gamma}(T)}_{:=\mathcal{T}_{\mathrm{Mn}}^{\gamma}}.$$

Similar to Eqn. 16, the austenite carbon-composition based on above Eqn. 17 is expressed as

$$c_{\mathrm{C}}^{\gamma} = \frac{1}{2D^{\gamma}} \left[\mu_{\mathrm{Mn}} - (2B^{\gamma} + 2D^{\gamma})c_{\mathrm{Mn}}^{\gamma} - \mathcal{T}_{\mathrm{Mn}}^{\gamma} \right]. \tag{18}$$

Equating the two expressions for phase-dependent carbon-concentration, Eqns. 16 and 18, the austenite manganese-composition is determined by

$$c_{\mathrm{Mn}}^{\gamma} = \frac{1}{2} \left[\frac{(\mu_{\mathrm{Mn}} - \mathcal{T}_{\mathrm{Mn}}^{\gamma})(A^{\gamma} + D^{\gamma}) - D^{\gamma}(\mu_{\mathrm{C}} - \mathcal{T}_{\mathrm{C}}^{\gamma})}{A^{\gamma}D^{\gamma} + A^{\gamma}B^{\gamma} + B^{\gamma}D^{\gamma}} \right]. \tag{19}$$

Furthermore, based on the carbon and manganese chemical potential, by writing the phase-dependent Mn-composition akin to Eqns. 16 and 16, the austenite carbon-concentration is calculated from

$$c_{\mathrm{C}}^{\gamma} = \frac{1}{2} \left[\frac{(\mu_{\mathrm{C}} - \mathcal{T}_{\mathrm{C}}^{\gamma})(B^{\gamma} + D^{\gamma}) - D^{\gamma}(\mu_{\mathrm{Mn}} + \mathcal{T}_{\mathrm{Mn}}^{\gamma})}{A^{\gamma}D^{\gamma} + A^{\gamma}B^{\gamma} + B^{\gamma}D^{\gamma}} \right]. \tag{20}$$

By ascertaining the austenite composition through the dynamic variables, μ_{C} and μ_{Mn}, its progressive change is tracked by monitoring the temporal evolution of the chemical potentials.

The change in the average carbon-composition in austenite during the growth of divergent pearlite at 625°C and 650°C is plotted in Fig. 5. Evidently, at both temperatures, the carbon content in the matrix decreases proportionately with time before gradually reaching the final composition. In other words, the predominantly linear decrease in the growth kinetics which accompany the transformations at 625°C and 650°C, as shown in Fig. 4, is governed by a similar change in the austenite carbon-concentration. Additionally, when compared to the sluggish change observed at the later stages of the transformation, the decrease in austenite carbon-concentration at 650°C is just marginally faster. A similar behaviour is noticeable in the correspondingly evolution of the kinetics in Fig. 4. Therefore, it is evident that the continuous decrease in matrix carbon-concentration predominantly exhibits a linear proportionality, which can be adopted to further
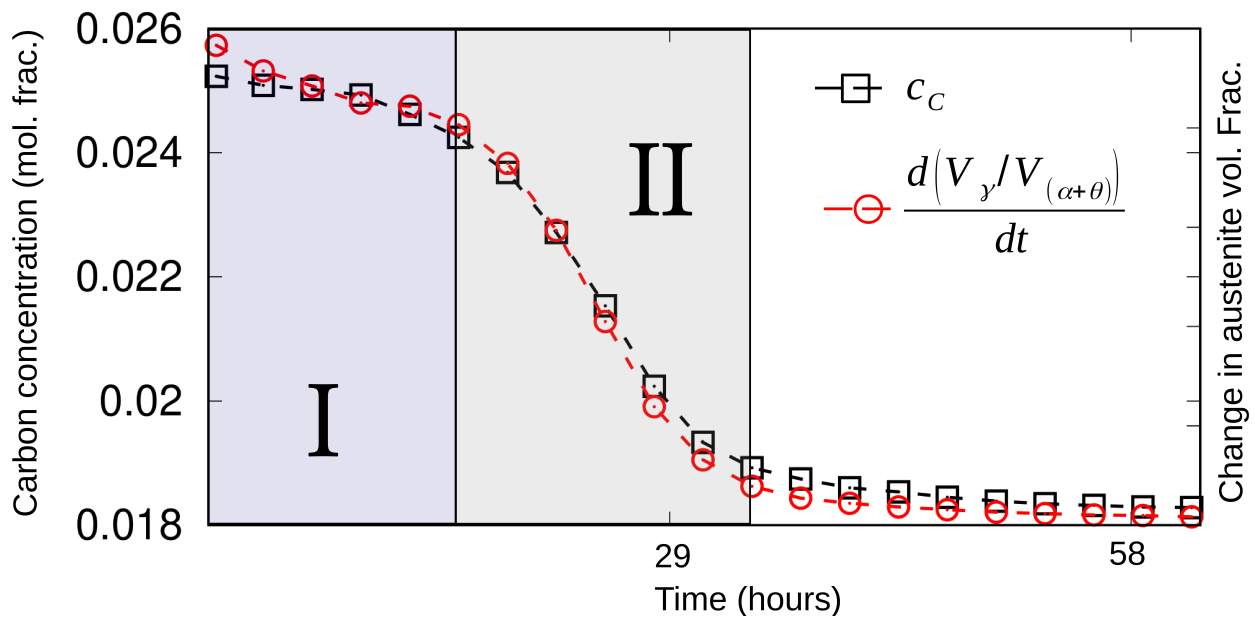
Figure 6: The temporal change in matrix carbon-content accompanying the eutectoid transformation at 605℃. As opposed to averaged growth-rate, austenite decomposition-rate is included in the plot. Based on the rate of change in the concentration (or decomposition rate), the decrease is distinguished into two segments.

analyse the non-stationary equilibrium characterising the pearlite transformation in the three-phase regime. Furthermore, Figs. 4 and 5 indicate that the trend exhibited by the temporally varying averaged growth-rate at 625℃ and 650℃ reflects the identical change in the austenite carbon-concentration.

The temporal evolution of the matrix carbon-composition associated with the larger undercooling, 605℃, is illustrated in Fig. 6. In contrast to the concentration change observed at 625℃ and 650℃, shown in Fig. 5, no significant decrease in carbon content is noticeable in the early stages of the isothermal transformation at 605℃. Moreover, the characteristic change in the austenite composition can be distinguished into two separate segments, as illustrated in Fig. 6, in addition to the final stage wherein the concentration decrease is gradual. In the first segment, which pertains to the initial stages of the transformation, the matrix carbon-content is seemingly unchanged. Under such unchanged composition, a steady-state transformation, which is distinguished by constant the growth kinetics, is expected. However, Fig. 4 indicates a decrease in averaged growth-rate from the onset of the austenite decomposition. To examine this counter-

18

intuitive outcomes, the change in the decomposition rate of austenite volume-fraction is monitored and included in Fig. 6. While the averaged transformation-kinetics indicate no steady-state evolution, the austenite decomposition-rate in Fig. 6 exhibits a temporal change which is consistent with the unchanged matrix composition in the early stages. The disparity between the austenite decomposition rate and the averaged growth-rate is introduced by the interfacial area which is included in Eqn.11. Fig. 2 shows that in the initial stages of the transformation at 605℃, owing to the relatively high transformation-kinetics, the phases assume a unique microstructure wherein 'valleys' are formed on either lateral boundaries of the domain. This microstructure, particularly in the early stages, causes a high interfacial area which increasingly reduces the averaged growth-rate, in accordance with Eqn.11. Therefore, a constant growth-rate is not observed in Fig. 4. However, by estimating the transformation rate without the influence of the interfacial area, kinetics in complete agreement with the concentration evolution is observed in Fig. 6. At higher undercooling, Fig. 6 indicates that the pearlite initially exhibits a steady-state growth before shifting to the non-stationary transformation kinetics which yield divergent pearlite. Similar to the austenite decomposition at 625℃ and 650℃, the non steady-state growth of the ferrite and cementite is characterised by the linear decrease in the matrix concentration, which is subsequently followed by a gradual change to equilibrium.

Based on the present analysis, it can be stated that the transition, with decrease in temperature, from a completely divergent growth of the pearlite, as in 650℃, to a predominantly steady-state transformation, which is often associated with the two-phase regime, is continuous. In other words, the amount of steady-state growth in the initial stages of the austenite decomposition is expected to increase with the decrease in temperature, such that when the condition eventually crossovers to the two-phase regime, the pearlite transformation primarily follows the conventional framework. Moreover, the transition from the steady state to the divergent growth, at a given temperature, can be attributed to a phenomenon akin to 'soft impingement'. Since rigorous investigation of this soft impingement is beyond the scope of the present work, it will be addressed in the upcoming studies.
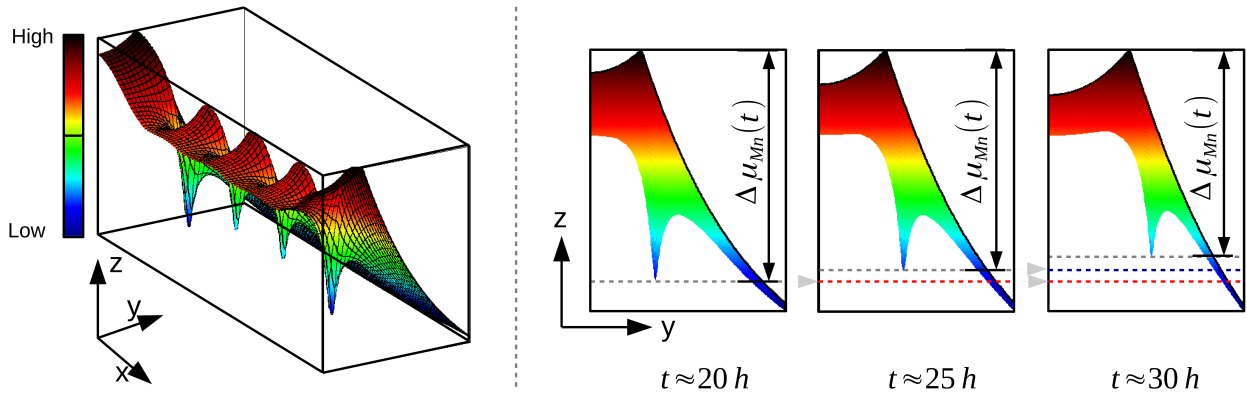
Figure 7: A three-dimensional depiction of the Mn chemical-potential around the growth-front of the divergent pearlite, is evolving at 625℃. The decrease in the potential-difference ($|\Delta\mu_{\mathrm{Mn}}(t)|$) which translates to the Mn partitioning driving-force is illustrated.

3.4. Manganese partitioning

Under the P-LE condition, the growth of the pearlite is governed by the partitioning of slow-diffusing manganese from ferrite to cementite [10, 14]. The driving-force which dictates this rate-governing manganese partitioning behavior can be formulated in various ways. Generally, based on the equilibrium conditions established across the ferrite- and cementite-austenite interface, the driving force is estimated as in Ref. [5]. When the equilibrium conditions change, the driving force for partitioning is consequently effected which ultimately leads to a change in the transformation kinetics. Since the current formulation adopts the chemical potential as the dynamic variable, the manganese partitioning is studied by examining the corresponding chemical potential.

A three-dimensional representation of the Mn chemical-potential at the pearlite growth-front of an isothermal transformation at 625℃ is rendered in Fig. 7. The peaks are the high-potential region associated with ferrite and the valleys are low-potential region pertaining to the cementite. Governed by the difference in the chemical potentials the manganese migrate from the ferrite to cementite. Therefore, the Mn potential-difference between the ferrite and cementite, at the growth front, governs the partitioning. In Fig. 7, the change in the potential difference with time is illustrated. As indicated by the illustration, the Mn potential-difference ($\Delta\mu_{\mathrm{Mn}}(t)$) decreases with the transformation, thereby reducing the overall growth rate.
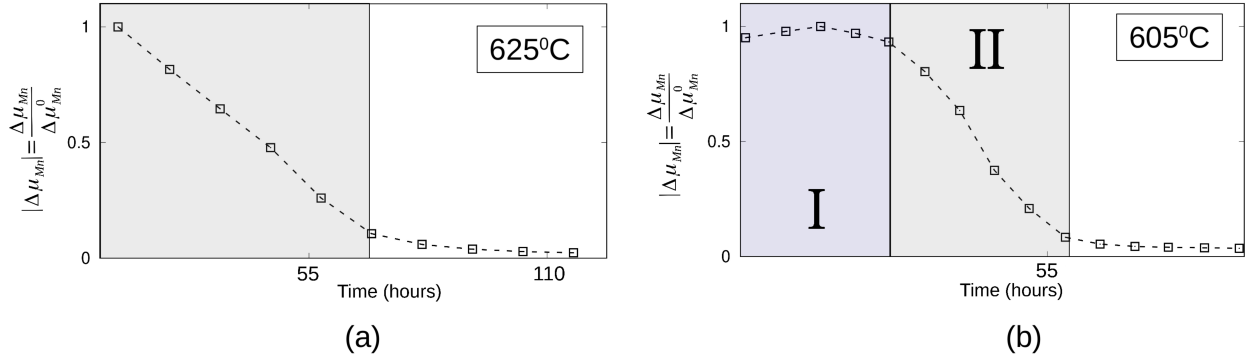
Figure 8: The change in the Mn partitioning driving-force with time during the eutectoid decomposition at a) 625°C and b) 605°C. Depending on the trend the decrease in the $\Delta\mu_{\mathrm{Mn}}(t)$ is distinguished into segments.

To understand the entire evolution of the Mn partitioning driving-force, the respective potential difference at various time-steps during the divergent growth at 625°C is estimated and plotted in Fig. 8a. The potential difference is normalised by considering the partitioning driving-force at the initial stage of the transformation ($|\Delta\mu_{\mathrm{Mn}}(t)| = \frac{\Delta\mu_{\mathrm{Mn}}(t)}{\Delta\mu_{\mathrm{Mn}}^{0}}$). In keeping with the proportional decrease in matrix composition, which accompanies the transformation at 625°C, the partitioning driving-force decreases linearly with time. Therefore, owing to the linear decrease in austenite carbon-concentration at 625°C, the Mn potential-difference proportionately reduces which consequently results in linear deceleration of the growth kinetics.

For the isothermal transformation at 605°C, the temporal change in the normalised Mn partitioning driving-force is shown in Fig. 8b. Similar to the concentration evolution, a segment wherein the Mn potential-difference is apparently constant is observed in the early stages of the transformation. The initial steady-state segment indicated by the constant partitioning driving-force, agrees with the duration when the matrix carbon-content and austenite decomposition-rate, as shown in Fig. 6, are temporally unchanged. Furthermore, the time-invariant potential difference in the initial stage is subsequently followed by a proportional change in the partitioning driving-force, which decreases the pearlite growth-rate.

Analysing Fig. 8, in relation to the temporal change in the matrix composition and the transformation kinetics, elucidated in Secs. 3.3 and 3.2, it is evident that the decrease in the carbon concentration influences the pearlite growth-rate by correspondingly reducing the partitioning

21

driving-force. Moreover, the trend in the concentration change is visibly reflected in evolution of the Mn potential-difference ($|\Delta\mu_{Mn}(t)|$) and the austenite decomposition-rate. Particularly, at higher undercooling, the steady-state growth of pearlite is associated with the unchanged partitioning driving-force before proportionally decreasing with time, akin to the transformation at 625°C.

3.5. Manganese gradient in cementite

The decrease in the matrix carbon-content, during the pearlite growth, while influencing the kinetics, changes the equilibrium condition established across the interface. As discussed in the previous section, this non-stationary equilibrium decreases the partitioning driving-force, thereby triggering a non-steady evolution of pearlite at all the temperatures considered. Although at 605°C, a segment of seemingly constant transformation kinetics is exhibited in the early stages, the evolution is predominantly dictated by the temporal decrease in the driving force. Experimentally, the non-stationary equilibrium condition which accompany the divergent-pearlite transformation is realised by periodically measuring the composition across the interface [18, 21]. These observations indicate that, as the transformation proceeds, the manganese content in the cementite increases. Apart from the one-dimensional spatial-variation in Mn concentration across the interface, the subsequent evolution of this concentration disparity, which is introduced by the non-stationary equilibrium, has not been expounded yet. To that end, the phase-dependent Mn composition is ascertained for the different undercoolings, as formulated in Sec. 3.3, and its distribution in cementite is illustrated in Fig. 9.

Irrespective of the transformation, the characteristic non steady-state equilibrium condition introduces an increase in the manganese composition along the growing direction of the cementite. Despite the time-dependent kinetics, which is invariably sluggish than the respective binary system, the gradient in the Mn concentration persists till the end of the transformation, as shown in Fig 9. Experimental investigations, analysing the discontinuous transformation over an extended duration, have identified non-uniform distribution in manganese in the bulk region, and long after the phase-fractions have reached the equilibrium [20]. Although, the concentration gradient in the constituent phase can be expected to dissipate after a prolonged period,
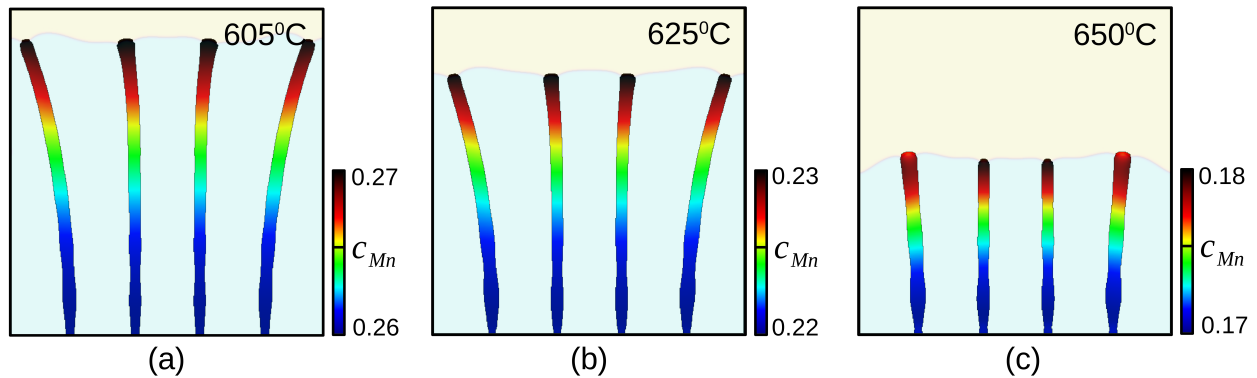
Figure 9: The distribution of manganese in cementite associate with divergent pearlite emerging from eutectoid decomposition at a) 605℃, b) 625℃ and c) 650℃.

releasing the time taken for the growth of the divergent pearlite, it is reasonable to assume that non-uniform distribution of the manganese are an integral part of this microstructure.

4. Conclusion

In the present numerical study, a phase-field technique which recovers the characteristic non-stationary partitioning local-equilibrium (P-LE) condition is employed to examine the factors governing the growth of the divergent pearlite in ternary Fe-C-Mn system. Consistent with the experimental observations, qualitatively, it is shown that the transformation kinetics linearly decrease as the evolution proceeds. This predominant linear decrease is subsequently followed by a gradual reduction in the growth rate, which ultimately results in the equilibrium phase-fractions.

Thermodynamically, the austenite carbon-concentration is deemed as the factor responsible for the non steady-state evolution. Therefore, the temporal change in the matrix composition is monitored in this theoretical analysis. It is identified that, for isothermal transformation at 625℃ and 650℃, the decrease in the austenite carbon-concentration is similar to the temporal change in the averaged growth-rate. However, at undercooling of 605℃, a definite duration wherein the matrix composition is unchanged is observed in the initial stages of the transformation. This time-invariant carbon concentration yields a steady-state decomposition rate, which is resolvable in the current consideration. Consistent with the characteristic evolution of the

matrix carbon-content, which varies with the degree of undercooling, it is shown that the Mn partitioning driving-force exhibit similar temporal variation. Since in the P-LE condition, the Mn partitioning dictates the transformation kinetics and the observed non-steady state growth rate. Moreover, the influence of the non-stationary equilibrium condition which accompanies the growth of the divergent pearlite, is explicated by examining the distribution of manganese in cementite. This analysis unravels that the temporally varying equilibrium condition establishes a Mn concentration gradient with the cementite, despite the sluggish rate of transformation.

Although, in the current work, the governing thermodynamic factors are analysed, the numerical framework does not explicitly include the role of the interface diffusion. Therefore, in the upcoming analyses, the combinatory influence of the different modes of diffusion on the transformation kinetics and the emerging microstructure will be investigated. Furthermore, attempts are being made to distinguish the lattice-occupancy of the alloying elements in the current phase-field approach. In subsequent works, quantitative conditions will additionally be incorporated by relaxing the simplifications pertaining to the equal interfacial energy-densities and anisotropic conditions [43, 44, 45].

Conflict of Interest

The authors declare that they have no conflict of interest.

Acknowledgments

References

References

[1] M De Graef, MV Kral, and Mats Hillert. A modern 3-d view of an "old" pearlite colony. *JOM*, 58(12):25–28, 2006.

[2] David Llewellyn and Roger Hudd. *Steels: metallurgy and applications.* Elsevier, 1998.

[3] N Ridley. The pearlite transformation. *Phase transformations in ferrous alloys*, pages 201–236, 1983.

[4] N Ridley. A review of the data on the interlamellar spacing of pearlite. *Metallurgical and Materials Transactions A*, 15(6):1019–1036, 1984.

[5] DE Coates. Diffusion controlled precipitate growth in ternary systems: Ii. *Metallurgical Transactions*, 4(4):1077–1086, 1973.

[6] Lars Onsager. Theories and problems of liquid diffusion. *Annals of the New York Academy of Sciences*, 46(5):241–265, 1945.

[7] JS Kirkaldy. Diffusion in multicomponent metallic systems: I. phenomenological theory for substitutional solid solution alloys. *Canadian Journal of Physics*, 36(7):899–906, 1958.

[8] JS Kirkaldy. Diffusion in multicomponent metallic systems: ii. solutions for two-phase systems with applications to transformations in steel. *Canadian Journal of Physics*, 36(7):907–916, 1958.

[9] GR Purdy. D. h, weichert and js kirkaldy. *Trans. metall. Soc. AIME*, 230:1025, 1964.

[10] M Hillert, HI Aaronson, DE Laughlin, RF Sekerka, and CM Wayman. Solid-solid phase transformations. *TMS±AIME, Warrendale, PA, USA*, pages 789–806, 1982.

[11] J Fridberg and M Hillert. Ortho-pearlite in silicon steels. *Acta Metallurgica*, 18(12):1253–1260, 1970.

[12] Makoto Kikuchi, Masanori Kajihara, and Si-Kyung Choi. Cellular precipitation involving both substitutional and interstitial solutes: cellular precipitation of cr2n in cr ni austenitic steels. *Materials Science and Engineering: A*, 146(1-2):131–150, 1991.

[13] CR Hutchinson and GJ Shiflet. The formation of partitioned pearlite at temperatures above the upper ae1 in an fe–c–mn steel. *Scripta materialia*, 50(1):1–5, 2004.

[14] DE Coates. Diffusional growth limitation and hardenability. *Metallurgical Transactions*, 4(10):2313–2325, 1973.

[15] JH Frye Jr, EE Stansbury, and DL McElroy. Absolute rate theory applied to rate of growth of pearlite. *Trans. AIME*, 197(219-224):3–47, 1953.

[16] N Ridley, D Brown, and HI Malik. Chemical metallurgy of iron and steel. *Iron and Steel Institute, London*, pages 268–71, 1973.

[17] ML Picklesimer, DL McElroy, TM Kegley, EE Stansbury, and JH Frye. Effect of manganese on the austenite-pearlite transformation. *TRANSACTIONS OF THE AMERICAN INSTITUTE OF MINING AND METALLURGICAL ENGINEERS*, 218(3):473–480, 1960.

[18] CR Hutchinson, RE Hackenberg, and GJ Shiflet. The growth of partitioned pearlite in fe–c–mn steels. *Acta materialia*, 52(12):3565–3585, 2004.

[19] John W Cahn and WG Hagel. Divergent pearlite in a manganese eutectoid steel. *Acta Metallurgica*, 11(6):561–574, 1963.

[20] Aleks YM Ontman and GJ Shiflet. Thermodynamic mapping of austenite decomposition's approach toward

equilibrium in fe−c−mn at 700° c. *Acta Materialia*, 89:98–108, 2015.

[21] MM Aranda, Rosalía Rementeria, J Poplawsky, E Urones-Garrote, and Carlos Capdevila. The role of c and mn at the austenite/pearlite reaction front during non-steady-state pearlite growth in a fe−c−mn steel. *Scripta Materialia*, 104:67–70, 2015.

[22] LT Mushongera, PG Kubendran Amos, B Nestler, and K Ankit. Phase-field simulations of pearlitic divergence in fe-c-mn steels. *Acta Materialia*, 150:78–87, 2018.

[23] MP Puls and JS Kirkaldy. The pearlite reaction. *Metallurgical and Materials Transactions B*, 3(11):2777–2796, 1972.

[24] Seong Gyoon Kim, Won Tae Kim, and Toshio Suzuki. Phase-field model for binary alloys. *Physical review e*, 60(6):7186, 1999.

[25] PG Kubendran Amos, LT Mushongera, and Britta Nestler. Phase-field analysis of volume-diffusion controlled shape-instabilities in metallic systems-i: 2-dimensional plate-like structures. *Computational Materials Science*, 144:363–373, 2018.

[26] Tobias Mittnacht, PG Kubendran Amos, Daniel Schneider, and Britta Nestler. Understanding the Influence of Neighbours on the Spheroidization of Finite 3-Dimensional Rods in a Lamellar Arrangement: Insights from Phase-Field Simulations. In *Numerical Modelling in Engineering*, pages 290–299. Springer, 2018.

[27] PG Kubendran Amos, Ephraim Schoof, Daniel Schneider, and Britta Nestler. On the volume-diffusion governed termination-migration assisted globularization in two-phase solid-state systems: Insights from phase-field simulations. In *Numerical Modelling in Engineering*, pages 47–63. Springer, 2018.

[28] Katsumi Nakajima, Markus Apel, and Ingo Steinbach. The role of carbon diffusion in ferrite on the kinetics of cooperative growth of pearlite: A multi-phase field study. *Acta Materialia*, 54(14):3665–3672, 2006.

[29] I Steinbach and M Apel. The influence of lattice strain on pearlite formation in fe−c. *Acta Materialia*, 55(14):4817–4822, 2007.

[30] Ramanathan Perumal, PG Kubendran Amos, Michael Selzer, and Britta Nestler. Phase-field study on the formation of first-neighbour topological clusters during the isotropic grain growth. *Computational Materials Science*, 140:209–223, 2017.

[31] Ramanathan Perumal, PG Kubendran Amos, Michael Selzer, and Britta Nestler. Phase-field study of the transient phenomena induced by 'abnormally' large grains during 2-dimensional isotropic grain growth. *Computational Materials Science*, 147:227–237, 2018.

[32] PG Kubendran Amos, LT Mushongera, Tobias Mittnacht, and Britta Nestler. Phase-field analysis of volume-diffusion controlled shape-instabilities in metallic systems-ii: Finite 3-dimensional rods. *Computational Materials Science*, 144:374–385, 2018.

[33] PG Kubendran Amos, Ephraim Schoof, Daniel Schneider, and Britta Nestler. On the globularization of the shapes associated with alpha-precipitate of two phase titanium alloys: Insights from phase-field simulations.

Acta Materialia, 159:51–64, 2018.

[34] PG Kubendran Amos, Avisor Bhattacharya, Britta Nestler, and Kumar Ankit. Mechanisms of pearlite spheroidization: Insights from 3d phase-field simulations. *Acta Materialia*, 161:400–411, 2018.

[35] Janin Tiaden, Britta Nestler, Hermann-Josef Diepers, and Ingo Steinbach. The multiphase-field model with an integrated concept for modelling solute diffusion. *Physica D: Nonlinear Phenomena*, 115(1-2):73–86, 1998.

[36] Mathis Plapp. Unified derivation of phase-field models for alloy solidification from a grand-potential functional. *Physical Review E*, 84(3):031601, 2011.

[37] J Eiken, B Böttger, and I Steinbach. Multiphase-field approach for multicomponent alloys with extrapolation scheme for numerical application. *Physical review E*, 73(6):066122, 2006.

[38] PG Amos. Understanding the volume-diffusion governed shape-instabilities in metallic systems. *arXiv preprint arXiv:1906.10404*, 2019.

[39] Robert F Mehl and William C Hagel. The austenite: pearlite reaction. *Progress in Metal Physics*, 6:74–134, 1956.

[40] AM Gokhale and RT DeHoff. Estimation of nucleation rate and growth rate from time dependence of global microstructural properties during phase transformations. *Metallurgical Transactions A*, 16(4):559–564, 1985.

[41] V Marx, FR Reher, and G Gottstein. Simulation of primary recrystallization using a modified three-dimensional cellular automaton. *Acta Materialia*, 47(4):1219–1230, 1999.

[42] Helena Magnusson, D Juul Jensen, and Bevis Hutchinsson. Growth rates for different texture components during recrystallization of if steel. *Scripta Materialia*, 44:435–441, 2001.

[43] Oleg Tschukin, Alexander Silberzahn, Michael Selzer, Prince GK Amos, Daniel Schneider, and Britta Nestler. Concepts of modeling surface energy anisotropy in phase-field approaches. *Geothermal Energy*, 5(1):19, 2017.

[44] PG Kubendran Amos, Ephraim Schoof, Nick Streichan, Daniel Schneider, and Britta Nestler. Phase-field analysis of quenching and partitioning in a polycrystalline Fe-C system under constrained-carbon equilibrium condition. *Computational Materials Science*, 159:281–296, 2019.

[45] PG Kubendran Amos, Ephraim Schoof, Daniel Schneider, and Britta Nestler. Chemo-elastic phase-field simulation of the cooperative growth of mutually-accommodating widmanstätten plates. *Journal of Alloys and Compounds*, 767:1141–1154, 2018.